

Resting-State Retinotopic Organization in the Absence of Retinal Input and Visual Experience

Andrew S. Bock,^{1,6} Paola Binda,² Noah C. Benson,^{1,3} Holly Bridge,⁴ Kate E. Watkins,^{4,5} and Ione Fine⁶

¹Department of Neurology, University of Pennsylvania, Philadelphia, Pennsylvania 19104, ²University of Pisa, Department of Translational Research on New Technologies in Medicine and Surgery, 56126 Pisa PI, Italy, ³Department of Psychology, New York University, New York, New York 10003, ⁴Functional MRI of the Brain Centre, Nuffield Department of Clinical Neurosciences, University of Oxford, John Radcliffe Hospital, Oxford, OX3 9DU, United Kingdom, ⁵Department of Experimental Psychology, University of Oxford, Oxford, OX1 3UD, United Kingdom, and ⁶Department of Psychology, University of Washington, Seattle, Washington 98177

Early visual areas have neuronal receptive fields that form a sampling mosaic of visual space, resulting in a series of retinotopic maps in which the same region of space is represented in multiple visual areas. It is not clear to what extent the development and maintenance of this retinotopic organization in humans depend on retinal waves and/or visual experience. We examined the corticocortical receptive field organization of resting-state BOLD data in normally sighted, early blind, and anophthalmic (in which both eyes fail to develop) individuals and found that resting-state correlations between V1 and V2/V3 were retinotopically organized for all subject groups. These results show that the gross retinotopic pattern of resting-state connectivity across V1-V3 requires neither retinal waves nor visual experience to develop and persist into adulthood.

Key words: blindness; cortical maps; fMRI; resting state; retinotopy; visual deprivation

Significance Statement

Evidence from resting-state BOLD data suggests that the connections between early visual areas develop and are maintained even in the absence of retinal waves and visual experience.

Introduction

Early visual deprivation disrupts ocular dominance column formation, receptive field size, and orientation, spatial frequency, direction, and disparity tuning (for review, see Hirsch and Leventhal, 1978; Movshon and Van Sluyters, 1981; Sherman and Spear, 1982; Rao and Jacobson, 2006; Ackman and Crair, 2014). In contrast, development of retinotopic organization is primarily driven by molecular signaling (Huberman et al., 2008; Cang and Feldheim, 2013). Retinotopic maps in the dorsal lateral geniculate nucleus and visual cortex of mice persist in the absence of retinal waves, although precision is reduced (Grubb et al., 2003; McLaughlin et al., 2003; Cang et al., 2005). In the macaque, adult-

like connections between V1 and V2 are present before birth, shortly after LGN axons reach layer IV (Coogan and Van Essen, 1996), although further refinement occurs with the onset of visual experience (Barone et al., 1995; Batardière et al., 2002; Baldwin et al., 2012).

Little is known about how these connections are affected by long periods of deprivation. Sight recovery subjects retain basic visual abilities after long periods of deprivation (Fine et al., 2003; Sikl et al., 2013), and retinotopic organization has been demonstrated in an adult sight recovery subject blinded at 3 years of age (Levin et al., 2010), yet it is not clear whether the retinotopic pattern of connections between early visual areas is maintained in early blind and anophthalmic (in which input from the optic nerves never exists or only exists temporarily early in development before the embryonic eyes degenerate) individuals.

Furthermore, early blind and anophthalmic individuals show occipital functional responses during auditory (e.g., Collignon et al., 2009; Watkins et al., 2013), tactile (Sathian and Stilla, 2010), language (Bedny et al., 2011; Watkins et al., 2012), and verbal memory (Amedi et al., 2003) tasks (for review, see Lewis and Fine, 2011). It is not known whether these cross-modal responses replace or coexist with retinotopic patterns of connectivity.

Received Nov. 15, 2014; revised June 24, 2015; accepted July 10, 2015.

Author contributions: A.S.B. and I.F. designed research; A.S.B., H.B., K.E.W., and I.F. performed research; N.C.B. contributed unpublished reagents/analytic tools; A.S.B., P.B., and I.F. analyzed data; A.S.B., P.B., H.B., K.E.W., and I.F. wrote the paper.

This work was supported by National Institutes of Health Grant R01 EY014645 to I.F., H.B. is a Royal Society University Research Fellow.

The authors declare no competing financial interests.

Correspondence should be addressed to either of the following: Dr. Andrew S. Bock, Department of Neurology, University of Pennsylvania, Philadelphia, PA 19104, E-mail: bock.andrew@gmail.com; or Dr. Ione Fine, Department of Psychology, University of Washington, Seattle, WA 98177, E-mail: ionefine@uw.edu.

DOI:10.1523/JNEUROSCI.4715-14.2015

Copyright © 2015 the authors 0270-6474/15/3512366-17\$15.00/0

Table 1. Selective summary of previous findings comparing the resting-state signals between blind and sighted individuals, including a description of which resting-state components would predict each finding^a

	Finding	Publication	Potential components	Comments
Within area correlations				
Fine-scale	V1-V3 cortico-cortico correlation modeled as a Gaussian point-spread function across millimeters of striate cortex Similar when accounting for the size of the cortical sheet*	Butt et al., 2013; Butt et al., 2015	Local or retinotopic	Consistent with any organization where response similarity falls off smoothly as a function of cortical distance, including the spatial spread inherent to the BOLD signal (Engel et al., 1997; Parkes et al., 2005)
Ipsilateral, across area				
Areal	Correlations higher between corresponding regions. Clustering algorithm could distinguish correlation patterns associated with upper versus lower visual field seeds Similar in blind and sighted subjects*	Butt et al., 2015; Striem-Amit et al., 2015	Local or retinotopic	
Eccentricity	Butt et al. (2015) found higher correlations between iso-eccentric regions of cortex. Striem-Amit et al. (2015) found a clustering algorithm could distinguish the patterns created from foveal versus peripheral seed ROIs Striem-Amit et al. (2015) found no overall differences between blind and sighted subjects. However, Butt et al. (2015) previously showed that, in early blind individuals, iso-eccentric correlations between corresponding regions had higher amplitude and spread more broadly, whereas the opposite pattern was found for homotopic regions*	Butt et al., 2015; Striem-Amit et al., 2015	Local and iso-eccentric, or retinotopic	Butt et al. (2015) found no evidence of polar angle organization within areas. The analyses by Striem-Amit et al. (2015) left this aspect of organization unexplored
Across-hemisphere correlations				
Areal	Across-hemisphere correlations weaker than within-hemisphere but stronger between cortical homologs. Striem-Amit et al. (2015) found that a clustering algorithm could distinguish correlations patterns from left versus right seed ROIs Across-hemisphere correlations are weaker in early blind individuals across occipital cortex, although no difference in clustering algorithm accuracy*	Butt et al., 2015; Striem-Amit et al., 2015	Local and bilaterally iso-eccentric	Inconsistent with retinotopic organization because it represents higher correlations between cortical areas representing symmetric regions of visual space. Butt et al. (2015) found no evidence of within-area polar angle organization
Eccentricity	Correlations enhanced for iso-eccentric regions Subtle differences blind and sighted*	Butt et al., 2015	Bilaterally iso-eccentric	

^aAll previous findings can be explained in terms of a combination of local and iso-eccentric components of the resting-state signal. Corresponding regions refer to those representing similar regions of visual space (e.g., left hemisphere V1v, V2v, and V3v). Homotopic regions refer to paired quarters of the same visual area (e.g., V2v and V2d). Cortical homologs refer to regions that represent symmetric regions of visual space (e.g., left and right V3v).

*Differences between blind and sighted subjects.

Here, we examine the effect of anophthalmia and early blindness on the organization of resting-state BOLD correlations in visual cortex of humans. Slow fluctuations in the BOLD signal measured at rest show correlations across brain regions (Hagmann et al., 2008; Greicius et al., 2009; Honey et al., 2009; Bowman et al., 2012), which are thought to partially reflect neural activity (Biswal et al., 1995; Greicius et al., 2003). The occipital resting-state signal contains several components, including the following: (1) local spatial correlations (Butt et al., 2013, 2015); (2) large-scale iso-eccentric fluctuations within and across hemispheres (Heinzle et al., 2011; Jo et al., 2012; Butt et al., 2013, 2015; Haak et al., 2013; Gravel et al., 2014; Raemaekers et al., 2014; Arcaro et al., 2015); and (3) a component that maps to retinotopic organization. The clearest evidence for retinotopic organization, which cannot be explained by the other components, is the reversal in polar angle on the V2/V3 border (Heinzle et al., 2011; Gravel et al., 2014; Raemaekers et al., 2014).

Previous studies have found local spatial correlations (Butt et al., 2013, 2015), higher correlations between cortical areas representing the same region of visual space (Butt et al., 2015; Striem-Amit et al., 2015), and higher correlations between iso-eccentric locations (Butt et al., 2015; Striem-Amit et al., 2015), in both blind and sighted subjects (Table 1; see Discus-

sion). However, these studies have not shown the V2/V3 polar angle reversal required to definitively demonstrate the retinotopic component of the resting-state signal persists following early blindness.

We examined the organization of resting-state signals across visual areas by estimating ipsilateral “connective fields,” the Gaussian region in V1 that best predicts the resting-state BOLD responses of seed voxels in V2 and V3 (Haak et al., 2013; Gravel et al., 2014). Correlations between resting-state signals across these visual areas were retinotopically organized in all subject groups, suggesting the retinotopic pattern of intrahemispheric resting-state connectivity across V1-V3 develops and persists in the absence of retinal waves and visual experience.

Materials and Methods

Subjects

Table 2 provides subject details. At the University of Washington, resting-state data were collected on early blind (rsEB_{UW}, $N = 5$, 2 females) and normally sighted controls (rsCON_{UW}, $N = 5$, 3 females). For the normally sighted control subjects, we also collected data while subjects passively viewed retinotopic mapping stimuli. At the University of Oxford, resting-state data were collected on anophthalmic subjects (rsANO_{Ox}, $N = 5$, 2 females) and control subjects (rsCON_{Ox}, $N = 7$, 5 females). Because resting-

Table 2. Subject details for anophthalmic and early blind individuals^a

Subject	Gender	Age (years)	Clinical description
AN01	Male	28	Bilateral anophthalmia associated with OTX2 mutation; mother carrier; delayed speech and motor development
AN02	Female	33	Isolated bilateral anophthalmia; no family history
AN03	Male	20	Isolated bilateral anophthalmia associated with dysplastic kidneys and mild systolic murmur; no family history
AN04	Female	21	Isolated bilateral anophthalmia, right with orbital cyst; no family history
AN05	Male	25	Isolated bilateral anophthalmia; no family history
AN06	Male	26	Isolated bilateral anophthalmia; no family history
EB1	Female	51	Retinopathy of prematurity; low light perception until retina detached at 25 years; 2 months premature
EB2	Male	60	Retinopathy of prematurity; no light perception; 2 months premature
EB3	Female	36	Retinopathy of prematurity; low light perception until 14 years; 2 months premature
EB4	Male	30	Leber's congenital amaurosis; low light perception
EB5	Male	38	Glaucoma from birth, light perception until 7 years in right eye, no light perception in left eye; unknown etiology, possible rubella virus in pregnancy

^aThe numbering of anophthalmic cases is consistent with that used in previous reports.

state data were collected in two locations using slightly different protocols, data from anophthalmic and early blind subject groups were only compared with normally sighted controls scanned in the same location using the same protocol. The study was approved by the University of Oxford and the University of Washington Institutional Review Boards, and all subjects provided written informed consent.

MRI

Oxford

Scans were acquired using a 3 tesla Siemens Trio with a 12-channel head coil. One or more anatomical images were acquired for each subject using a standard T1-weighted, high-resolution anatomical scan of MP-RAGE (192 axial slices, 192×192 matrix, $1 \times 1 \times 1$ mm³, TR = 2.04 s, TE = 4.7 ms, TI = 900 ms, FA = 8°). An independent components analysis of these resting-state data has been published previously (Watkins et al., 2012).

Resting-state. Echo planar BOLD fMRI data were collected with whole-brain coverage (180 volumes; 34 axial slices, 64×64 matrix, $3 \times 3 \times 3.5$ mm³, TR = 2.1 s, TE = 28 ms, FA = 89°, descending slice acquisition). Functional scans were obtained in a dark room with subjects instructed to keep their eyes closed.

University of Washington

Scans were acquired using a 3 tesla Philips Achieva with a 32-channel head coil. One or more anatomical images were acquired for each subject using a standard T1-weighted, high-resolution anatomical scan of MP-RAGE (176 slices, 256×256 matrix, $1 \times 1 \times 1$ mm³, TR = 2.2 s, TE = 3.5 ms, TI = 896.45 ms, FA = 7°).

Resting-state. Echo planar BOLD fMRI data were collected with whole-brain coverage (160 volumes, 43 axial slices, 80×80 matrix, $3 \times 3 \times 3$ mm³, TR = 2.4 s, TE = 25 ms, FA = 79°, ascending slice acquisition). Functional scans were obtained in a dark room with subjects instructed to keep their eyes closed.

Stimulus-driven. Echo planar BOLD fMRI data were collected with whole-brain coverage (160 volumes, 43 axial slices, 80×80 matrix, $3 \times 3 \times 3$ mm³, TR = 2.4 s, TE = 25 ms, ascending slice acquisition). Functional scans were obtained while subjects maintained fixation on a central fixation cross. Visual stimuli were generated using MATLAB and the PsychToolbox (Brainard, 1997; Pelli, 1997) and back-projected by a calibrated LCD projector on a screen mounted in the bore of the magnet, which subjects viewed via a mirror fixed on the coil. fMRI responses were measured using a 2 degree drifting bar stimulus (as in Dumoulin and Wandell, 2008). For all sequences, the stimulated areas contained a counter-phase flickering checkerboard pattern (100% contrast, 0.5 cycles per degree) modulating at 8 Hz, and the display region was an annular aperture extending from 0.25 to 8 degrees eccentricity.

In the stimulus-driven dataset, it is presumed that BOLD modulations over time were driven by both spontaneous BOLD fluctuations and by the neural response to the time-varying stimulus. The stimulus-driven component should be retinotopically organized, as regions that represent similar regions in space show similar stimulus-driven responses over time. This dataset therefore provides a demonstration of our ability to estimate connective fields in the presence of a known retinotopic component. With this

motivation in mind, connective fields for the stimulus-driven data were generated in the same way as the resting-state data.

Image preprocessing

Brain surfaces were reconstructed and inflated from the MP-RAGE images using the FreeSurfer (version 5.1) toolkit (<http://surfer.nmr.mgh.harvard.edu/>) as described previously (Dale et al., 1999; Fischl et al., 1999). Raw echo planar (volumetric) data were motion corrected with a six parameter, least-squares rigid body realignment routine, using the first functional image as a reference, and sinc interpolated in time to correct for the slice acquisition sequence using SPM (Wellcome Trust Centre for Neuroimaging, University College London, London). There were no significant differences in head motion across groups (mean rms head motion \pm SD: rsANO_{OX} = 0.2911 ± 0.3748 ; rsCON_{OX} = 0.0948 ± 0.0850 ; rsEB_{UW} = 0.1557 ± 0.0431 ; rsCON_{UW} = 0.1362 ± 0.0390 ; stimCON_{UW} = 0.1392 ± 0.0501). A one-way ANOVA revealed no differences in head motion across groups ($F_{(1,4)} = 0.81$, $p = 0.5334$).

Following motion and slice timing correction, the echo planar data in subject space were coregistered (without interpolation) to a subject-specific anatomy in FreeSurfer using FSL-FLIRT with 6 df under a FreeSurfer wrapper (bbregister). Physiological noise was removed based on techniques of Jo et al. (2010). White matter, gray matter, ventricle, and nonbrain tissue ROIs were identified in each subject's anatomical image using Freesurfer and were subsequently projected to functional space. White matter, ventricle, and nonbrain tissue ROIs were eroded in 3D by 1 voxel to avoid any partial volume contamination by gray matter.

The influence of the average time courses for these three "noise ROIs" was removed from each gray matter voxel time course using linear regression. After noise removal, gray matter voxel time courses were high-pass filtered (0.01 Hz). A low-pass filter was not used because of concerns that low-pass filters have the potential to reduce sensitivity and induce artificial correlations in both task-related (Skudlarski et al., 1999; Della-Maggiore et al., 2002; Strother, 2006) and resting-state (Davey et al., 2013) fMRI data. Time courses were then projected to the corresponding (left or right) native cortical surface. The gray and black time courses in Figure 1C represent time courses before and after noise removal.

Cortico-cortico receptive field fitting

Seed voxels were selected from a large occipital ROI containing V2 and V3 (based on Freesurfer cortical parcellation), selected for each subject in native surface space. Connective fields for these seed voxels were estimated using custom software in MATLAB (The MathWorks), implementing a method closely related to that described by Haak et al. (2013). The connective field of each seed voxel within V1 (Fig. 1A) was modeled using a Gaussian function, $g(v, \sigma)$ with two parameters: v_0 and σ as follows:

$$g(v) = \exp - [d(v, v_0)^2 / 2\sigma^2]$$

where $d(v, v_0)$ is the shortest distance along the cortical surface mesh between voxels v (all V1 voxels in this case) and the connective field

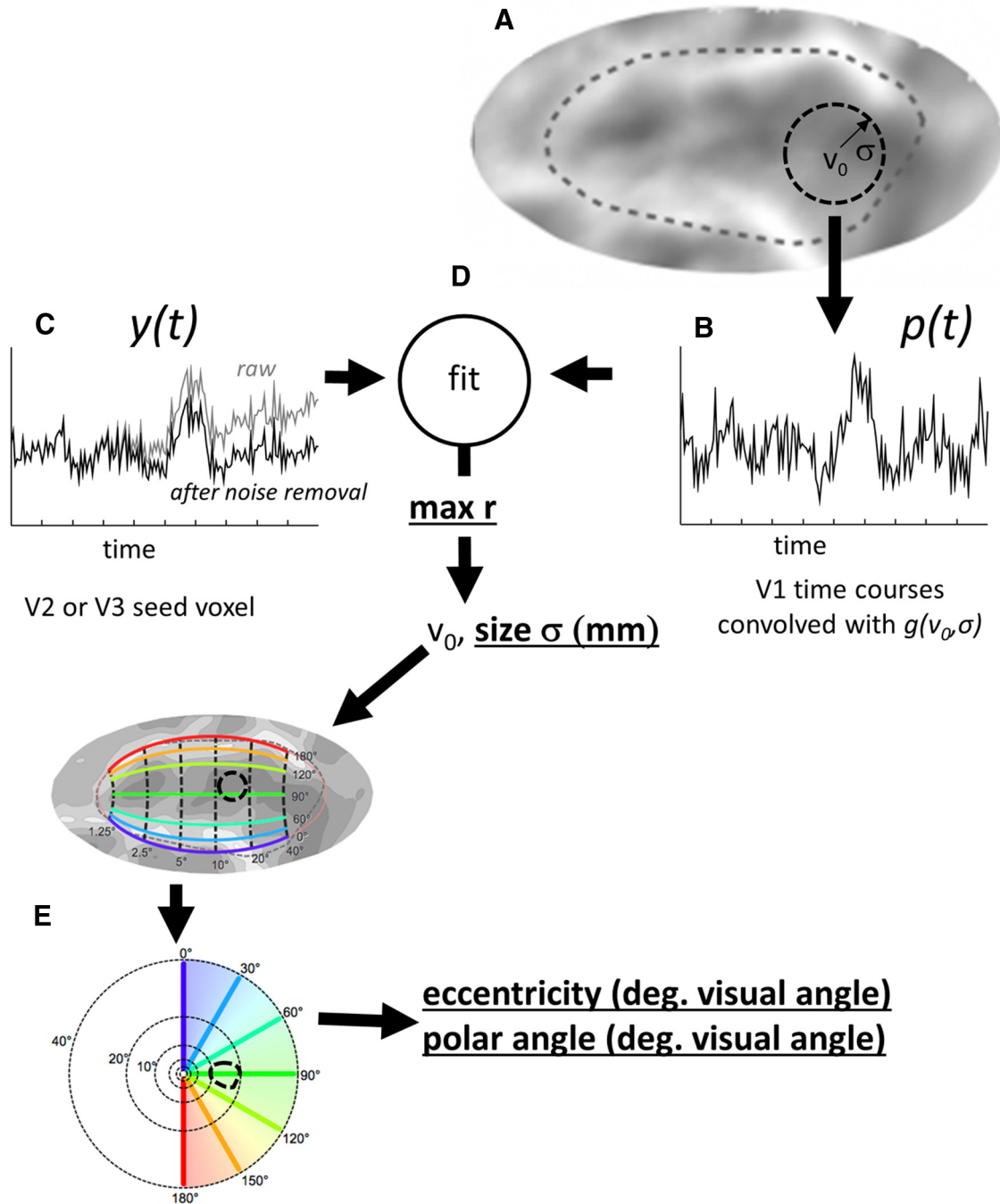


Figure 1. Schematic estimating the connective field for a seed voxel in V2 or V3. As described by Haak et al. (2013), assuming a linear relationship between blood-oxygenation levels and the fMRI signal, a predicted BOLD time course, $p(t)$, can be calculated using a parametrized model of the connective field. **A**, The circular symmetric Gaussian model, g , is defined by its projection on a three-dimensional mesh representation of the boundary between the gray and white matter of the brain. Parameters consist of the Gaussian center location, v_0 (in voxel coordinates) and the Gaussian spread, σ (in millimeters) across the folded cortical surface. **B**, The predicted BOLD time course, $p(t)$, for any seed voxel is obtained by convolving the connective field, $g(v_0, \sigma)$, with the fMRI time course signals in V1. The connective field model parameters that best predict (C) the observed BOLD time course, $y(t)$, are found by (D) maximizing the correlation coefficient between the prediction, $p(t)$, and the observed time series, $y(t)$. **E**, The parameter v_0 is converted into visual space coordinates via the Benson template model of early visual areas (Benson et al., 2014). Parameters examined in this paper (r , σ , eccentricity, and polar angle) are bold underlined.

center v_0 , computed using the “graphshortestpath” function in MATLAB (using Dijkstra’s algorithm). The parameter σ is the SD (mm) along the cortical surface.

We began by creating a set of fixed basis functions for each V1 voxel. These basis functions were described as Gaussians $g(v_0, \sigma)$ with center v_0 corresponding to the surface vertex closest to that V1 voxel at the gray/white matter border. For each v_0 value, we created 10 basis functions, using σ values linearly spaced between 3 and 25 mm. A series of predicted time courses were created for each V2 and V3 seed voxel by taking the linear sum

of all V1 time courses convolved with all possible basis functions (Fig. 1B). The connective field for each V2/V3 voxel was initially defined as the parameters of the basis function $g(v_0, \sigma)$ that maximized the correlation between that V2/V3 voxel’s time course and the resulting predicted time course. Initialization using this fixed set of σ values was critical for reducing the impact of local minima. It also had the advantage of shortening search time and excluding voxels with weak response modulation (for which the correlation with the initialization parameters was <0.1 ; under the assumption of linearity, this corresponds to a R^2 of 0.01). This stage may also have helped

reduce the effect of bilateral symmetric resting-state components (Raemaekers et al., 2014).

The parameters of $g(v_0, \sigma)$ were then used to initialize a nonlinear search procedure (MATLAB simplex algorithm), which manipulated σ to maximize the correlation between the predicted and observed fMRI response time courses, holding v_0 constant (Fig. 1C,D).

Conversion into visual space coordinates using the Benson template

Once the best fitting connective field was identified, connective field maps were projected to the corresponding hemisphere of a common FreeSurfer surface template (fsaverage) using the FreeSurfer spherical registration system (Fischl et al., 1999; Greve et al., 2011). The Benson template (2014) (details below) was used to convert v_0 into retinotopic polar angle and eccentricity coordinates represented in terms of degrees of visual angle (Fig. 1E). This template was originally created for the left hemisphere, so we projected it onto the right hemisphere.

Seed voxels were excluded from further processing if they originated outside the Benson V1-V3 template (Fig. 2, dotted outlines). Unless otherwise stated, data were thresholded to only include connective fields for which the correlation between predicted and observed fMRI responses was >0.1 (set a priori). A similar pattern of results was found for all the results described below (including the phase reversal) for a more stringent threshold of 0.2.

The Benson template is not validated against older or blind subjects, and both age (Hogstrom et al., 2013) and early visual deprivation led to a small reduction in cortical folding (Dehay et al., 1989, 1996). However, the expected effect of a misaligned Benson template would be to reduce correlations, increase mean squared differences between predictions and the retinotopic template, and reduce the V2/V3 reversal effect, regardless of which direction the boundary is misaligned. Thus, misalignment of the template cannot contribute to our finding of retinotopically organized polar angle connective field estimates in blind individuals. Inspection of individual data found no evidence of systematic misalignment.

ROI selection

Areas V1-V3 were defined using an anatomical template of Benson et al. (2014), which uses surface topology to predict both polar angle and eccentricity. This template accurately predicts the location and retinotopic organization of V1 (Benson et al., 2012) or V1-V3 (Benson et al., 2014) in sighted subjects from cortical anatomy alone.

V2 and V3 ROIs were further partitioned into three equal subregions (“foveal,” “middle,” and “peripheral”) as a function of eccentricity based on the Benson template. The boundaries, which were chosen to produce equal numbers of voxels within each eccentricity band, were 5.5 and 18.9 degrees eccentricity for the left hemisphere, and 5 and 18.6 degrees for the right hemisphere. These two ROIs also correspond to the region of the template that has been empirically validated based on stimulus-driven retinotopic maps. The most peripheral boundary represented 18.6/18.9–83 degrees eccentricity, corresponding to the greatest eccentricity value represented in the Benson template.

ROIs were also partitioned into dorsal and ventral subregions. Ventral subregions were defined as those with a template polar angle value >90 (representing the upper visual field in normally sighted individuals); dorsal subregions were defined as those with a template polar angle value <90 (representing the lower visual field in normally sighted individuals).

Model of local resting-state correlations

We also compared our polar angle estimates with a model based purely on local spatial correlations in the resting-state signal, using parameters based on a previous study of resting-state fMRI (Butt et al., 2013). Random time courses were created across the entire cortical surface (using MATLAB's `randn` function). Local spatial correlations were then induced by smoothing these random time courses on the cortical surface using a 30 mm kernel. This produced simulated resting-state correlations on the cortical surface whose point spread of local spatial correlations (converted into z-scores) was best modeled by a Gaussian with σ of 20 mm, the value observed by Butt et al. (2013). Additional random noise was then added with an amplitude 200% of the original time course

variance, so as to produce connective fields with median correlation coefficients of 0.292, similar to those observed in subject data (see below). Results using this model proved robust to a wide range of added noise (0%–2000% was tested). Cortico-cortico receptive field fitting (as described above) was carried out on these simulated time courses.

Statistics

Bootstrapping

As distributions of connective field values were non-normal, statistical comparisons adopted a nonparametric approach. Comparisons of frequency distributions of connective field parameter values across groups were performed using a bootstrapping procedure using custom software, based on the χ^2 test of independence. This test compares the obtained frequency distributions for each group with those that would be obtained if the frequency distribution of connective field parameter values was independent of group assignment. We began with a classic χ^2 test of independence, in which the obtained frequencies of the parameter value of interest were compared with the expected frequency distribution of connective field parameter values was independent of group assignment. Thus, a large χ^2 value suggests that group membership influences the distribution of values obtained for that parameter (McHugh, 2013). The significance of the χ^2 value was estimated using a bootstrapping procedure, which simply reestimated χ^2 after randomly assigning subjects to groups (10,000 simulations). Significance was estimated as the probability of shuffled χ^2 values exceeding the real χ^2 . Subjects (rather than voxels or hemispheres) were randomly assigned between groups.

When comparing distributions across the two hemispheres, we again randomly assigned subjects (rather than voxels) across groups, making this bootstrap procedure the equivalent of a random-effects analysis.

Comparing individual subject data to the Benson template/local correlations (LC) model

Eccentricity and polar angle connective field values in V2/V3 were compared with the V2/V3 values found in the Benson anatomical surface template, as well as the model based on local resting-state correlations, using R^2 and mean squared difference (MSD) values.

MSD between the Benson template and individual data was calculated as follows for each individual hemisphere: $MSD_{Benson} = \frac{1}{n} \sum_{i=1}^n (p - p_{Benson})^2$, where n is the number of voxels and p is the connective field parameter value of interest for each voxel. The MSD between the LC model and subject data was similarly calculated as follows: $MSD_{LC} = \frac{1}{n} \sum_{i=1}^n (p - p_{LC})^2$.

The significance of R^2 or MSD values was estimated using a bootstrapping procedure, where the real distribution of R^2 or MSD values was compared with simulated distributions created using random assignment of subjects across the two groups (10,000 simulations). Once again, simulating bootstrapped distributions by randomly assigning subjects (rather than voxels) across groups made this bootstrap procedure the equivalent of a random-effects analysis.

Multiple comparisons

Correction for multiple comparisons was performed using Bonferroni–Holm correction (Holm, 1979), a sequentially rejective version of a simple Bonferroni correction for multiple comparisons, which controls the family-wise error rate at level α .

Results

Figure 2 shows the four parameters that represent our connective field model on the left hemisphere surface, averaged across all members of each subject group. The V2/V3 ROI used for analyses is shown with a dotted line. Figure 2A shows correlation coefficients. These provide a measure of the fit of the connective field model. Any deterioration in retinotopic organization might lead to a reduction in spatially local correlated neural firing, and thereby reduce correlation coefficients. Figure 2, B and C, shows eccentricity and polar angle

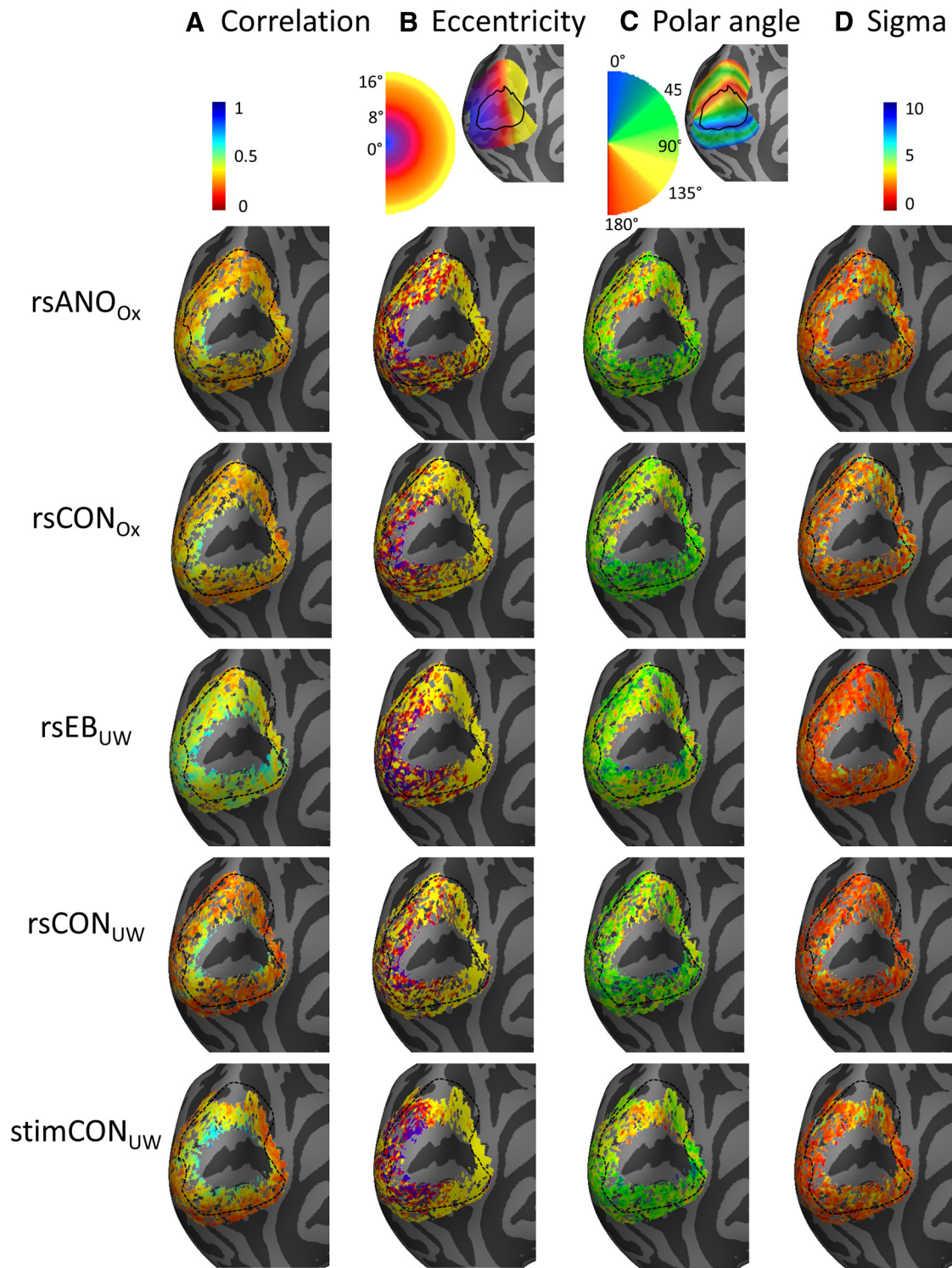


Figure 2. Connective field parameters of interest for V2/V3 on the surface of the left hemisphere, averaged across all members of each subject group. The V2/V3 ROI used in analyses is shown as a dotted outline. Columns from left to right represent the following: (A) the correlation between predicted and obtained time courses, (B) estimated eccentricity, (C) estimated polar angle, and (D) estimated σ (connective field size, mm on the cortical surface). Rows represent parameter estimates for resting-state anophthalmic subjects (Oxford), resting-state normally sighted Oxford controls, early blind subjects (UW), resting-state normally sighted UW controls, and normally sighted UW controls viewing retinotopic mapping stimulus sequences. The legend shows color coding for each subject/hemisphere. Top insets, Expected mappings for eccentricity and polar angle within V2 and V3 based on the Benson et al. (2014) template, with V1 outlined in black.

parameters (in degrees of visual angle), respectively. These parameters provide a way of examining whether the match between connective field location and that predicted by retinotopic organization is disrupted by blindness. Finally, Figure 2D shows connective field size estimates (in millimeters). Ex-

pansion of connective field sizes might be expected if visual deprivation resulted in either an increase in receptive field size or a reduction in the precision of retinotopic organization, as increased scatter in receptive fields might serve to increase connective field size (Dumoulin and Wandell, 2008).

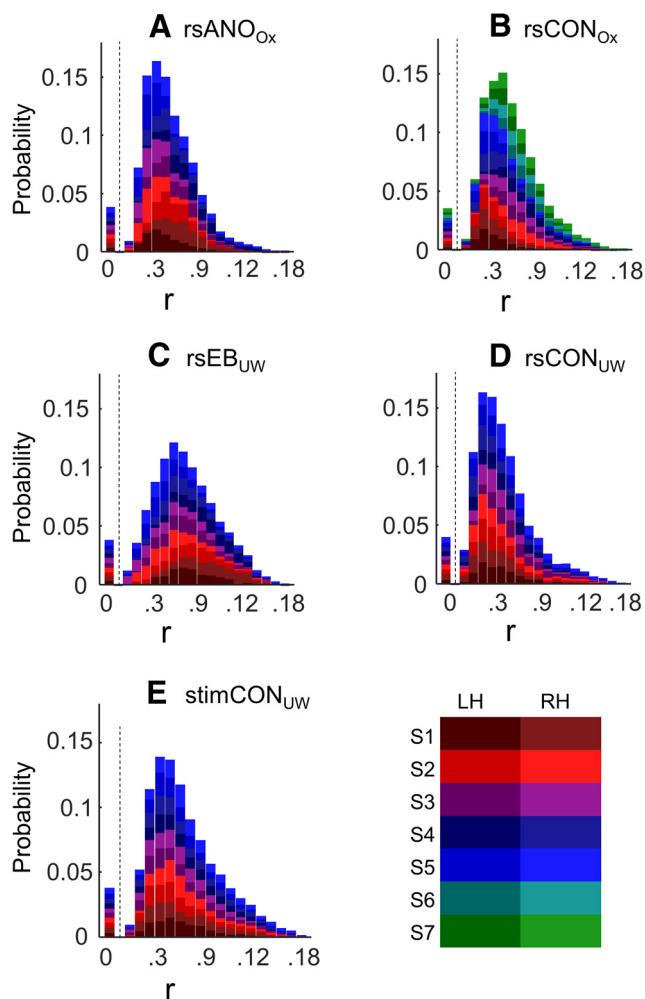


Figure 3. Probability density distributions of connective field correlation coefficients (r). Each color in the stacked histogram represents a separate individual hemisphere. The legend shows color coding for each subject/hemisphere. The distribution of correlation coefficients for each hemisphere was normalized to sum to 1, so each hemisphere and subject contributes equally to the plot. Data are the following: (A) resting-state anophthalmic subjects (Oxford), (B) resting-state normally sighted controls (Oxford), (C) early blind subjects (UW), (D) resting-state normally sighted controls (UW), and (E) normally sighted controls (UW) viewing retinotopic mapping stimulus sequences.

Correlation coefficients

Correlation coefficients were examined using an ROI that consisted of both V2 and V3. Our goal was to test for differences in correlation coefficients across groups, as might be expected if neural connectivity between V1 and V2/V3 was less precise or disrupted in blind individuals. We also wanted to make sure our threshold of 0.1 did not mask differences across subject groups.

Figure 3 shows probability distributions of correlation coefficients for all five subject groups. Each color in the stacked histogram represents the V2/V3 ROI in a separate individual hemisphere. The distribution of correlation coefficients for each hemisphere was normalized to sum to 1, so each hemisphere and subject contributes equally to the plot. A relatively small proportion of voxels were excluded because their connective field correlation coefficients fell below the threshold of 0.1 (percentage excluded: rsANO_{Ox} = 8.74%; rsCON_{Ox} = 8.12%; rsEB_{UW} = 10.74; rsCON_{UW} = 14.05; stimCON_{UW} = 10.39%). Two-tailed Wilcoxon rank-sum tests did not find any significant differences across subject groups in the number of excluded voxels

Table 3. Group differences for connective field correlation coefficients in V2/V3 ROI

Group comparison	χ^2	p
ANO _{Ox} versus rsCON _{Ox}	$\chi^2_{(1,5)} = 1083.198$	0.699
rsEB _{UW} versus rsCON _{UW}	$\chi^2_{(1,4)} = 15739.389^{**}$	0.009 ^{**}
rsCON _{UW} versus stimCON _{UW}	$\chi^2_{(1,4)} = 5108.558^*$	0.041 [*]

*Significant values.

**Statistical values that passed Bonferroni–Holm correction for three comparisons.

(rsANO_{Ox} vs rsCON_{Ox}: $t_{(21)} = -0.824$, $p = 0.419$; rsEB_{UW} vs rsCON_{UW}: $t_{(18)} = 1.013$, $p = 0.325$; rsCON_{UW} vs stimCON_{UW}: $t_{(18)} = -1.417$, $p = 0.174$). Excluded voxels are shown as having a correlation of 0 in Figure 3.

Median correlation coefficients were ~ 0.3 , corresponding to $R^2 = 0.09$ under an assumption of linearity (median values: rsANO_{Ox} = 0.304; rsCON_{Ox} = 0.324; rsEB_{UW} = 0.403; rsCON_{UW} = 0.282; stimCON_{UW} = 0.337). Bootstrapped tests of χ^2 independence (random effects) on the distribution of correlation coefficients that passed threshold found no effect of hemisphere on the distribution of correlation coefficients for any subject group.

We did see differences across groups for the distribution of correlation coefficients that passed threshold (Table 3). Bootstrapped χ^2 tests of independence revealed that correlation coefficients were significantly higher for early blind subjects than for their sighted controls. The reason for this is not entirely clear (see Discussion). However, the finding that blind subjects had equal (or higher) correlation values than sighted subjects suggests that the use of a 0.1 threshold did not “bias” our results toward finding equivalent retinotopic organization in anophthalmic and early blind subjects, as might be the case if fewer retinotopically organized voxels passed threshold in these groups.

Correlation coefficients were also significantly higher for stimulus-driven compared with resting-state data (Fig. 3; Table 3), although this did not pass correction for multiple comparisons. This finding is likely due to the enhanced signal provided by the stimulus-driven neural fluctuations (see Discussion).

Eccentricity

Eccentricity estimates differ between foveal, middle, and peripheral ROIs

Connective field eccentricity estimates were also examined using an ROI consisting of both V2 and V3. Because χ^2 estimates fail when a large number of cells have low expected probabilities, bin sizes were logarithmically distributed across the possible range of eccentricities when carrying out bootstrapped tests of χ^2 independence for eccentricity. No difference between left and right hemispheres was found on the distribution of connective field eccentricity estimates for any subject group.

Figure 4 shows probability distributions of eccentricity estimates for all five subject groups for foveal, middle, and peripheral ROIs. The idealized histograms, estimated from the Benson template, are shown as insets for each column. Eccentricity values fall off with an approximately exponential distribution, as predicted by cortical magnification (Engel et al., 1997; Dougherty et al., 2003; Duncan and Boynton, 2003). If connective field estimates were “perfect,” the histogram for each ROI would fall completely within the shaded region. Indeed, connective field estimates collected for stimulus-driven data fell almost perfectly into the shaded region for foveal and middle ROIs. Connective field estimates for the peripheral ROI fall outside the shaded region. This is likely due to the fact that the retinotopic stimuli were presented within a visual field of 8° radius; thus, the region of visual field corresponding to this peripheral ROI did not receive visual stimulation.

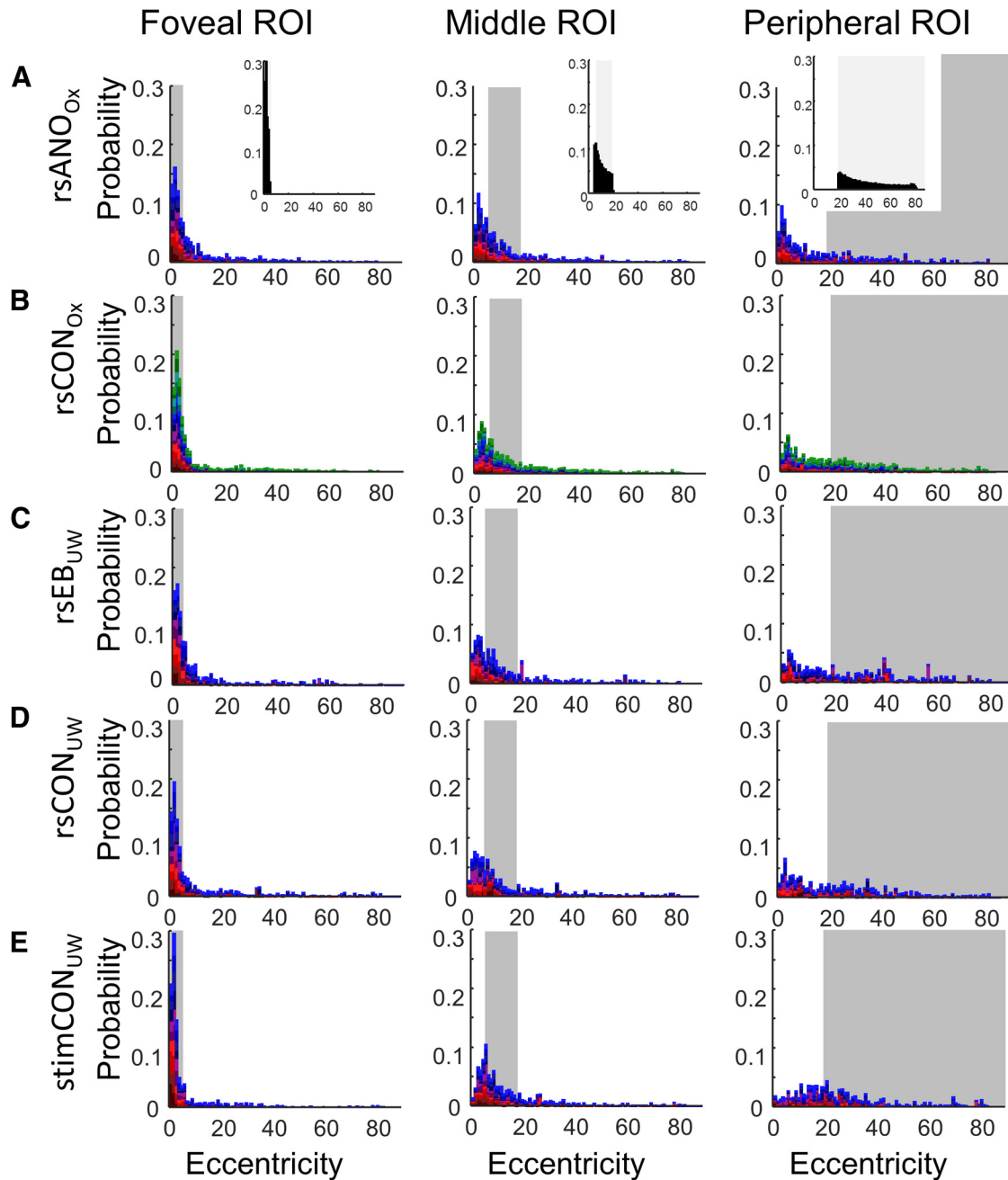


Figure 4. Probability density distributions of connective field eccentricity parameters. Each color in the stacked probability distribution represents a separate hemisphere (see legend of Fig. 3). Data are the following: (A) resting-state anophthalmic subjects (Oxford), (B) resting-state normally sighted controls (Oxford), (C) early blind subjects (UW), (D) resting-state normally sighted controls (UW), and (E) normally sighted controls (UW) viewing retinotopic mapping stimulus sequences. Shaded regions represent the eccentricity boundaries for the V2/V3 foveal, middle, and peripheral ROIs, respectively. Top insets, Expected probability distributions for eccentricity within V2 and V3 based on the Benson et al. (2014) template.

Although most apparent for stimulus-driven data, connective field estimates were smaller for foveal compared with middle ROIs, as well as smaller for middle compared with peripheral ROIs, for all subject groups. The distribution of connective field eccentricity estimates differed significantly across both the foveal versus middle ROIs and between middle versus peripheral ROIs for all subject groups except rsCON_{UW} (Table 4). Thus, eccentricity estimates followed the distribution of connective field eccentricity the expected general pattern of organization.

Table 5 examines group differences in the distribution of eccentricity values. There was a significant difference between anophthalmic subjects and their sighted controls for the foveal

ROI, but this did not pass correction for multiple comparisons. Visual inspection of the data of Figure 4 revealed that the peak in the foveal ROI probability distributions was shifted toward slightly larger eccentricity values in anophthalmic subjects compared with their sighted controls. If real, this difference in distributions might be interpreted as demonstrating a shallower slope for foveal cortical magnification.

Comparison of eccentricity estimates with the retinotopic model
 Finally, we compared connective field eccentricity parameters with Benson et al. (2014) template estimates of eccentricity, using both correlation coefficients (R^2) and MSDs. The two measures

Table 4. Connective field eccentricity estimates in V2/V3 ROI: foveal versus middle, and middle versus peripheral ROIs

Group	Foveal versus middle ROIs		Middle versus peripheral ROIs	
	χ^2	p	χ^2	p
rsANO _{ox}	$\chi^2_{(1,4)} = 1377.269^{**}$	0.032 ^{**}	$\chi^2_{(1,4)} = 1735.637^{**}$	0.02 ^{**}
rsCON _{ox}	$\chi^2_{(1,6)} = 8954.597^{**}$	0.001 ^{**}	$\chi^2_{(1,6)} = 2959.368^{**}$	0.01 ^{**}
rsEB _{uw}	$\chi^2_{(1,4)} = 4388.848^{**}$	0.000 ^{**}	$\chi^2_{(1,4)} = 4355.152^{**}$	0.007 ^{**}
rsCON _{uw}	$\chi^2_{(1,4)} = 6099.938^{**}$	0.000 ^{**}	$\chi^2_{(1,4)} = 2899.321$	0.079
stimCON _{uw}	$\chi^2_{(1,4)} = 15443.383^{**}$	0.000 ^{**}	$\chi^2_{(1,4)} = 7425.274^{**}$	0.009 ^{**}

^{**}Statistical values that passed Bonferroni–Holm correction for five comparisons.

Table 5. Group differences for connective field eccentricity estimates in V2/V3 ROI

Group	ROI	χ^2	p
ANO _{ox} versus rsCON _{ox}	Foveal	$\chi^2_{(1,5)} = 1474.206^*$	0.018
	Middle	$\chi^2_{(1,5)} = 944.341$	0.205
	Peripheral	$\chi^2_{(1,5)} = 1201.786$	0.115
rsEB _{uw} versus rsCON _{uw}	Foveal	$\chi^2_{(1,4)} = 1461.18$	0.367
	Middle	$\chi^2_{(1,4)} = 990.669$	0.743
	Peripheral	$\chi^2_{(1,4)} = 1095.507$	0.667
rsCON _{uw} versus stimCON _{uw}	Foveal	$\chi^2_{(1,4)} = 2088.069$	0.056
	Middle	$\chi^2_{(1,4)} = 1041.681$	0.443
	Peripheral	$\chi^2_{(1,4)} = 2913.646$	0.051

*Significant value.

Table 6. Group differences for MSD and R^2 values comparing connective field eccentricity estimates to the Benson et al. (2014) template

Group	Metric	Z value	p
ANO _{ox} versus rsCON _{ox}	R^2	−1.200	0.230
	MSD	1.142	0.254
rsEB _{uw} versus rsCON _{uw}	R^2	0.794	0.427
	MSD	−0.416	0.678
rsCON _{uw} versus stimCON _{uw}	R^2	−2.835 ^{**}	0.005 ^{**}
	MSD	2.608 ^{**}	0.009 ^{**}

^{**}Statistical values that passed Bonferroni–Holm correction for three comparisons.

differ slightly in their interpretation. MSD values represent the deviation between our obtained connective field values and the values predicted by the template. In contrast, high R^2 values can be obtained even if the slope of cortical magnification differs from the slope predicted from the Benson template, as might be the case if the Benson template underestimated or overestimated cortical magnification in blind individuals. Correlations between eccentricity estimates from the connective field model and the Benson et al. (2014) template were significantly positive ($p < 0.01$, Bonferroni–Holm correction for five comparisons) for all individual subjects (rsANO_{ox}: median $R^2 = 0.041$, rsCON_{ox}: median $R^2 = 0.081$, rsEB_{uw}: median $R^2 = 0.152$; rsCON_{uw}: median $R^2 = 0.087$; stimCON_{uw}: median $R^2 = 0.1510$).

Correlation coefficients (after a Fisher z-score transform) and MSD values were compared across groups using unsigned Wilcoxon rank sum tests (Table 6). Neither test found differences between anophthalmic or early blind subjects and their sighted controls, but correlation coefficients were significantly higher for stimulus-driven compared with resting-state data, presumably due to visual stimuli eliciting a neural response, which enhances the retinotopic component of the fMRI signal.

Thus, in all subject groups, our data show connective fields of V2/V3 mapping to iso-eccentric locations in V1, as would be expected if resting-state signals reflect retinotopic organization. However, it is important to note that, as discussed below, other groups have noticed a bilateral symmetric signal within the early visual areas, which, although nonretinotopic, would predict a

very similar outcome (Heinzle et al., 2011; Jo et al., 2012; Butt et al., 2013, 2015; Haak et al., 2013; Gravel et al., 2014; Arcaro et al., 2015). Thus, the presence of mapping for eccentricity is necessary but not sufficient to demonstrate a retinotopic component within the resting-state signal.

Polar angle

As discussed more fully below, eccentricity and σ parameters closely resembling those that would be expected to arise from retinotopic organization can also manifest from a combination of local spatial correlations in the resting-state signal (Butt et al., 2013), and a global bilaterally symmetrical signal consisting of enhanced correlations between iso-eccentric regions (Raemaekers et al., 2014), which may arise from vasculature that symmetrically stems from the posterior cerebral artery (Tong et al., 2013; Tong and Frederick, 2014). Correspondence between polar angle parameter values and expected retinotopic organization is therefore critical for demonstrating that our connective fields are at least partially driven by correlations in neural firing that reflect retinotopic organization.

Polar angle estimates differ between dorsal and ventral ROIs

Figures 5 and 6 show probability distributions of polar angle estimates for all five subject groups for dorsal and ventral ROIs in V2 and V3, respectively. The Benson template for V1 is mirror symmetric, such that 0 represents the left horizontal median for right V1 and the right horizontal meridian for left V1. Consequently, polar angle estimates for left and right hemispheres can be combined without further transformation. Bootstrapped tests of χ^2 independence did not find any difference between left and right hemispheres on the distribution of V2 and V3 connective field polar estimates for either ventral or dorsal ROIs for any subject group.

As seen from the inset (based on the Benson template), ventral ROI connective field estimates of polar angle should be distributed between 0 and $\pi/2$, whereas dorsal ROI estimates of polar angle should be distributed between 0 and $-\pi/2$. Bootstrapped tests of χ^2 independence (Table 7) found that in V2 the distribution of connective field polar angle estimates differed significantly across ventral and dorsal ROIs for all subject groups. In V3 differences across ventral and dorsal ROIs only reached significance in Oxford resting-state control subjects, and this did not survive correction for multiple comparisons.

The only group differences found for the distribution of connective field polar angle estimates were within V2d (rsANO_{ox} vs rsCON_{ox}: $\chi^2_{(19)} = 915.879$, $p = 0.042$; rsCON_{uw} vs stimCON_{uw}: $\chi^2_{(19)} = 1203.594$, $p = 0.004$). Only the difference between stimulus-driven and resting-state data passed Bonferroni–Holm correction for three comparisons.

Polar angle values within V2 and V3

We then examined the distribution of connective field estimates of polar angle within V2 and V3. Voxels within V2 and V3 were binned based on their expected polar angle representation using the Benson template. The mean connective field polar angle value for each bin is shown with solid symbols in Figure 7 (left panels). Because neither the Benson template nor the LC model incorporates hemispheric differences, we treated each hemisphere as a separate “subject,” so SEs reflect individual hemispheres. Connective field polar angle values predicted by the Benson template are shown with a solid line. Connective field polar angle values produced by a model of LC are shown with empty circles. As might be expected, connective fields in the LC model often have

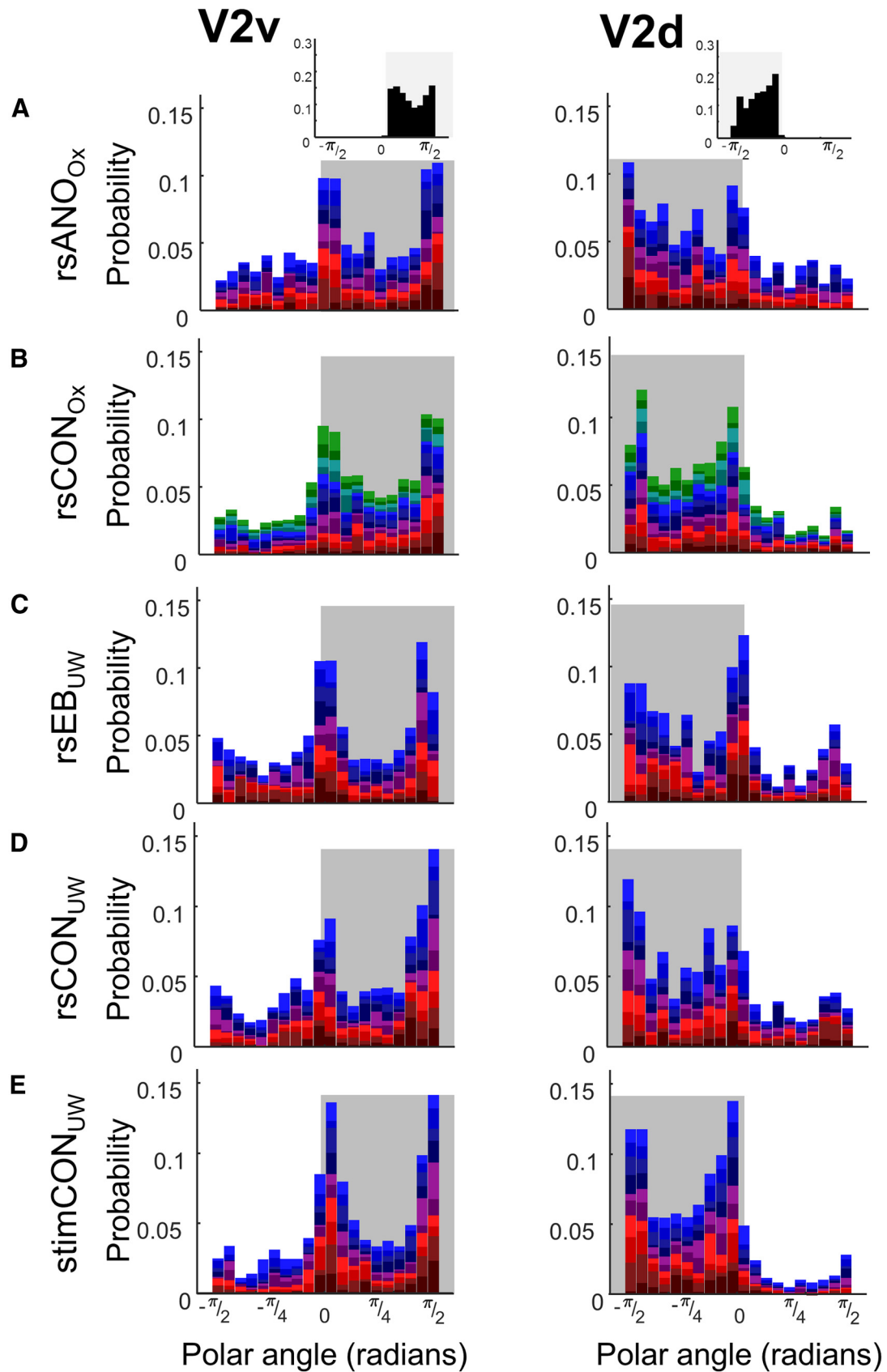


Figure 5. Probability density distributions of connective field polar angle parameters for V2v and V2d. Data are the following: (A) resting-state anophthalmic subjects (Oxford), (B) resting-state normally sighted controls (Oxford), (C) early blind subjects (UW), (D) resting-state normally sighted controls (UW), and (E) normally sighted controls (UW) viewing retinotopic mapping stimulus sequences. Shaded regions represent expected polar angle boundaries for dorsal and ventral ROIs. Top insets, Expected probability distributions for polar angle within V2 and V3 based on the Benson et al. (2014) template.

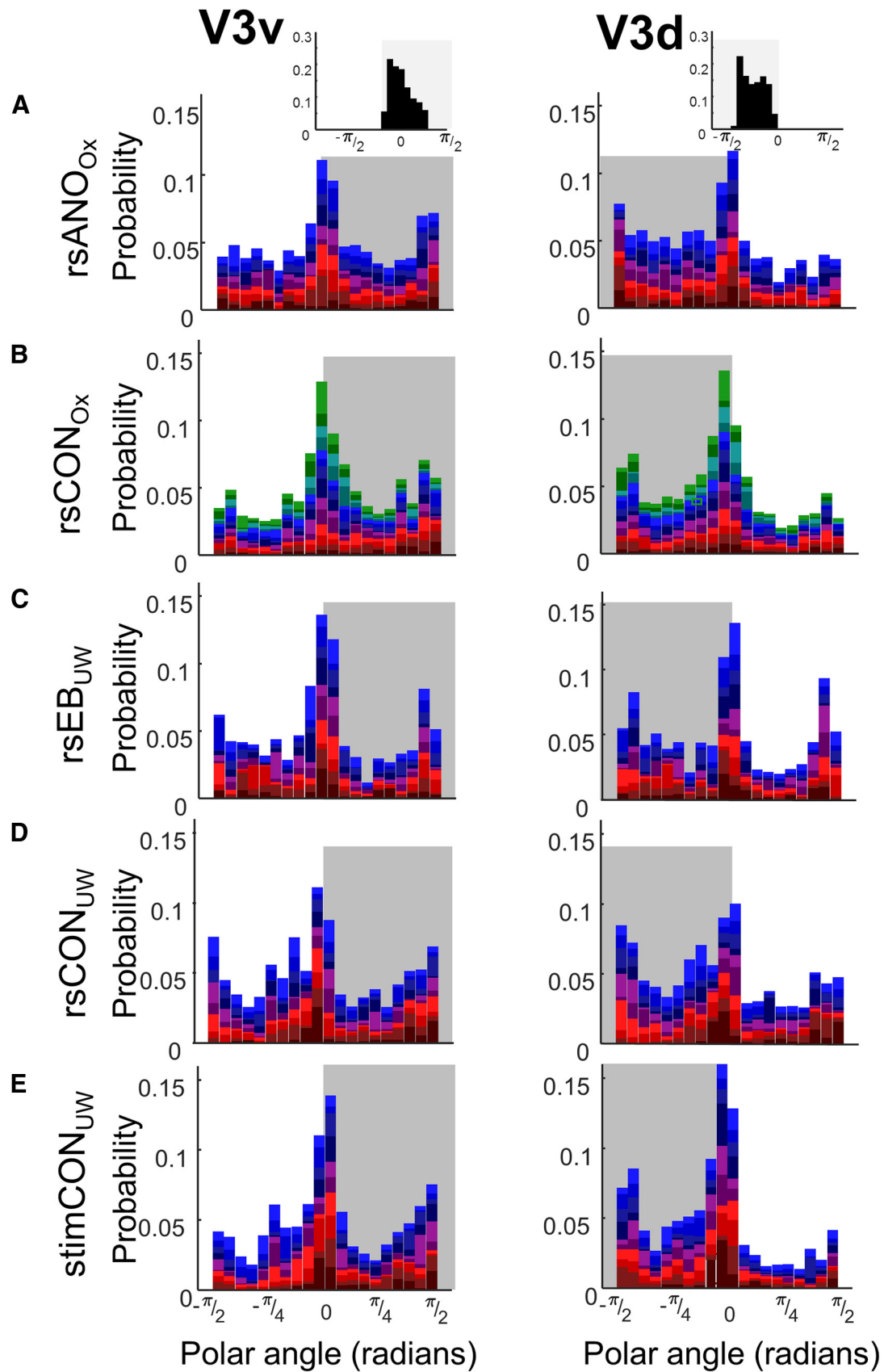


Figure 6. Probability density distributions of connective field polar angle parameters for V3v and V3d. Data are the following: (A) resting-state anophthalmic subjects (Oxford), (B) resting-state normally sighted controls (Oxford), (C) early blind subjects (UW), (D) resting-state normally sighted controls (UW), and (E) normally sighted controls (UW) viewing retinotopic mapping stimulus sequences. Shaded regions represent polar angle boundaries for dorsal and ventral ROIs. Top insets, Expected probability distributions for polar angle within V2 and V3 based on the Benson et al. (2014) template.

Table 7. Connective field polar angle estimates: ventral versus dorsal for V2 and V3

Group	V2v versus V2d		V3v versus V3d	
	χ^2	p	χ^2	p
rsANO _{Ox}	$\chi^2_{(1,4)} = 4121.51^{**}$	0	$\chi^2_{(1,4)} = 1021.029$	0.105
rsCON _{Ox}	$\chi^2_{(1,6)} = 8266.387^{**}$	0	$\chi^2_{(1,6)} = 1662.99$	0.028
rsEB _{UW}	$\chi^2_{(1,4)} = 2412.968^{**}$	0.012	$\chi^2_{(1,4)} = 645.725$	0.83
rsCON _{UW}	$\chi^2_{(1,4)} = 4464.518^{**}$	0	$\chi^2_{(1,4)} = 566.247$	0.719
stimCON _{UW}	$\chi^2_{(1,4)} = 9668.524^{**}$	0	$\chi^2_{(1,4)} = 1948.731$	0.054

**Statistical values that passed Bonferroni–Holm correction for five comparisons.

Table 8. Correlations between connective field polar angle estimates and the Benson et al. (2014) template for V2 and V3

Group	Metric	V2		V3	
		Median	p	Median	p
rsANO _{Ox}	R^2/Z	0.106/0.338**	0.002**	0.015/0.121**	0.002**
rsCON _{Ox}	R^2/Z	0.160/0.423**	0**	0.029/0.173**	0**
rsEB _{UW}	R^2/Z	0.052/0.232**	0.002**	0.001/0.038	0.432
rsCON _{UW}	R^2/Z	0.182/0.455**	0.002**	0.005/0.07	0.375
stimCON _{UW}	R^2/Z	0.236/0.531**	0.002**	0.031/0.177**	0.006**

**Statistical values that passed Bonferroni–Holm correction for five comparisons.

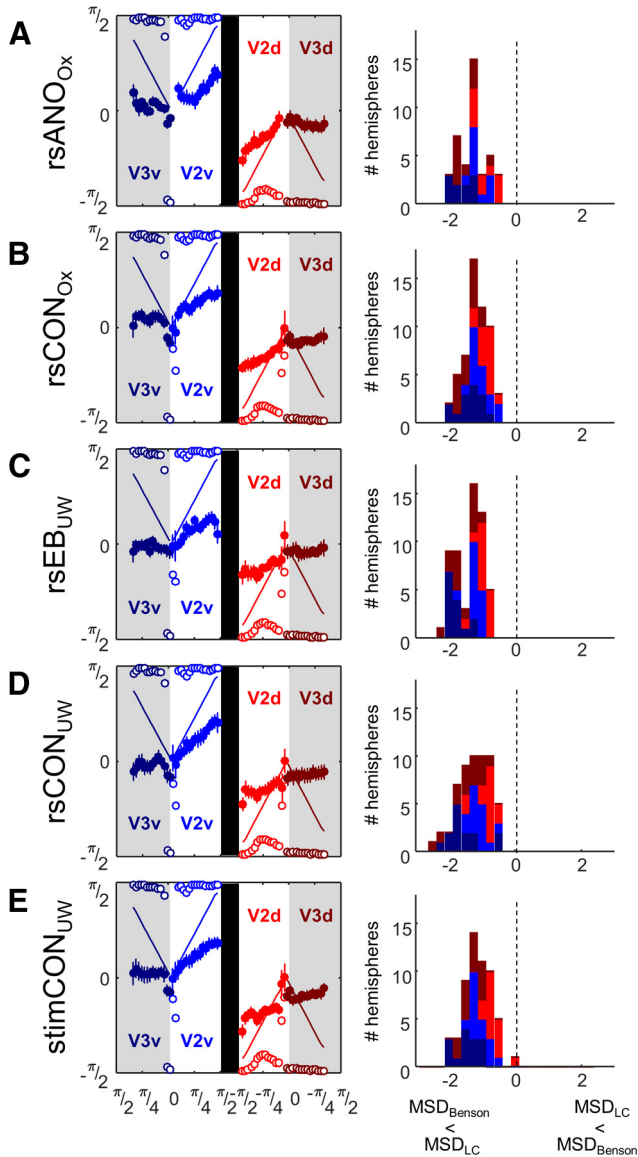


Figure 7. Left panels, Connective field estimates of polar angle for all 5 subject groups. Data are the following: (A) resting-state anophthalmic subjects (Oxford), (B) resting-state normally sighted controls (Oxford), (C) early blind subjects (UW), (D) resting-state normally sighted controls (UW), and (E) normally sighted controls (UW) viewing retinotopic mapping stimulus sequences. Voxels were binned based on their expected polar angle representation, using the Benson template. Solid symbols represent means across individual hemispheres. SEs across individual hemispheres are shown. Solid lines indicate predicted mean connective field estimates of polar angle based on the Benson template. Open circles represent predicted estimates based on the LC model. Right panels, Histograms of $MSD_{Benson} - MSD_{LC}$ for each individual subject hemisphere. Negative values (left of the dotted line) imply that the Benson template provides a better fit than the LC model.

the same polar angle as the closest V1 location, resulting in polar angle estimates clustered at $\pm \pi/2$. This “step” pattern was seen for a variety of noise levels (60%–1000% of time course variance).

Connective field estimates within both V2 and V3 were closer to the predictions of the Benson template than the LC model. The x -axes of the histograms of Figure 7 (right panels) represent $MSD_{Benson} - MSD_{LC}$. Thus, negative values represent a better fit by the Benson template compared with the LC model. Wilcoxon signed rank tests found that the median of the distribution of MSD across individual hemispheres was significantly smaller for the Benson template for all subject groups ($p < 0.001$).

Last, we explicitly looked for the expected reversal across the V3/V3 border. In V2, the median of the distribution of correlation values (transformed into z -scores) between individual subject hemisphere polar angle estimates and the Benson template was significantly (Wilcoxon signed rank test) greater than zero for all groups (Table 8).

Correlations with the template were lower in V3 than V2, especially V3d. This is not surprising: the Benson template is less accurate for V3 than V2 (Benson et al., 2014). Moreover, retinotopic mapping tends to be less robust dorsally than ventrally, and is less robust in V3 than within V2. Within V3, we found significantly positive correlations between subject data and the Benson template for anophthalmic subjects, Oxford sighted controls, and UW sighted subjects viewing retinotopic stimuli. The failure to find significantly positive correlations within V3 for early blind subjects and their sighted controls is likely due to lower signal-to-noise within the University of Washington scanner rather than a genuine difference between early blind and anophthalmic subjects, given that it was found in both subject groups.

Given the complexity of the resting-state signal in early visual areas, which likely includes bilateral symmetrical fluctuations that can produce the artifactual appearance of eccentricity mapping, a critical finding of our data is that we can successfully find the polar angle reversal at the V2/V3 border using resting-state as well as stimulus-driven data: at least in anophthalmic subjects, their sighted controls, and UW stimulus-driven control subject data. This reversal is a strong test of retinotopic organization, as it is difficult to think of any realistic model of spatial or vascular correlations that would predict such a finding.

Connective field size

No difference between left and right hemispheres was found on the distribution of connective field size estimates for any subject group for either the V2 or the V3 ROI. To improve our ability to sample the joint probability distribution describing connective field size and eccentricity, each hemisphere was treated as a separate “subject” rather than carrying out separate analyses for left and right hemispheres.

Figure 8 shows the joint probability distribution for connective field size and eccentricity, for each subject group for V2 and

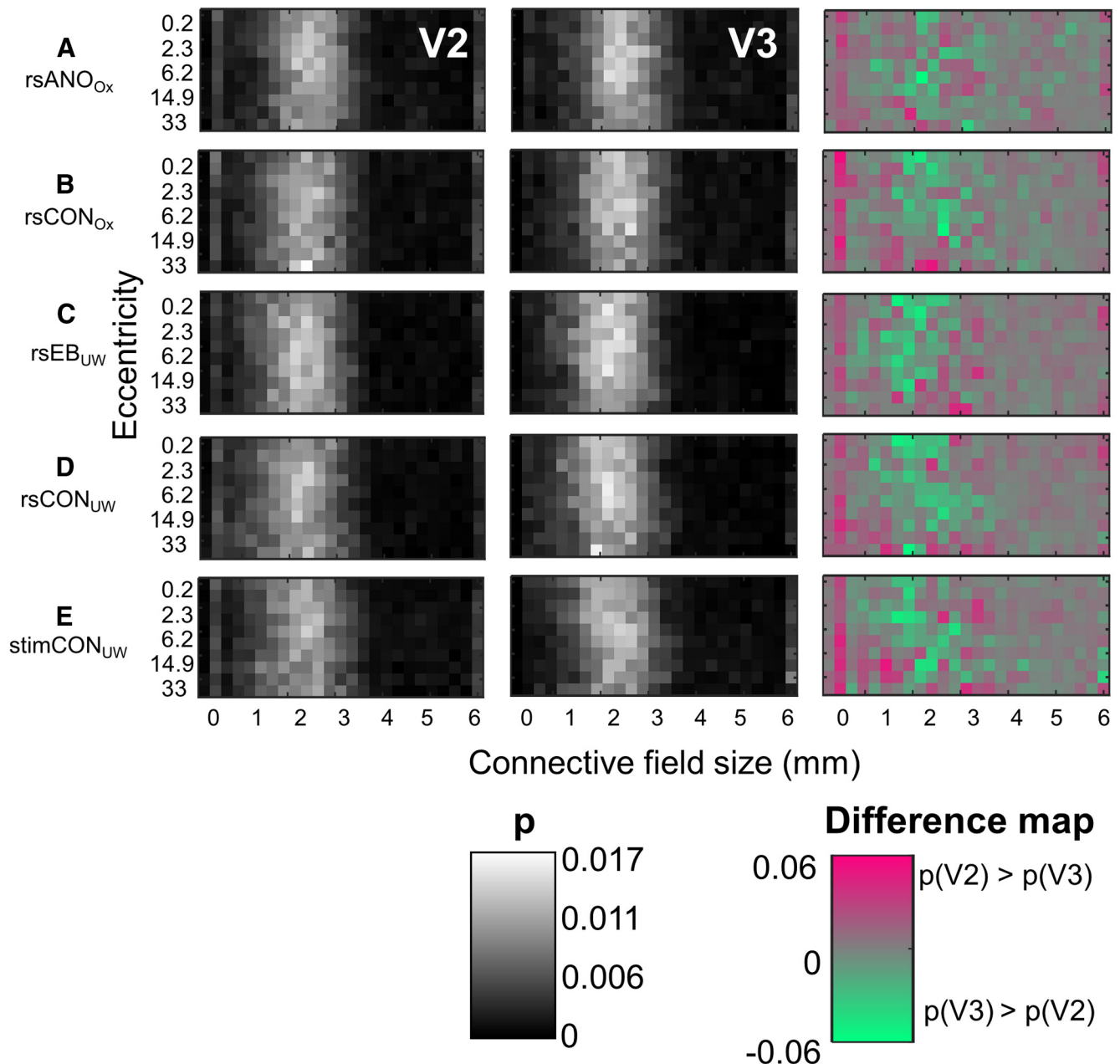


Figure 8. Two-dimensional joint probability distributions (x -axis, connective field size; y -axis, eccentricity) of connective field size as a function of eccentricity for V2 and V3. Data are the following: (A) resting-state anophthalmic subjects (Oxford), (B) resting-state normally sighted controls (Oxford), (C) early blind subjects (UW), (D) resting-state normally sighted controls (UW), and (E) normally sighted controls (UW) viewing retinotopic mapping stimulus sequences. The third column represents the differences between the joint histograms of V2 and V3. For reasons of visualization, the range of connective field sizes is limited to 0° – 6° .

V3. Because χ^2 estimates fail when a large number of cells have low expected probabilities, bin sizes for eccentricity were unevenly distributed across the range of possible sizes (bin widths of 0.25 between 0 and 3, widths of 0.5 between 3 and 6, and widths of 3 between 6 and 15 mm). Results were robust to the particular choice of bin sizes.

Differences in connective field sizes between V2 and V3

The resting-state connective field sizes shown in Figure 8 are very similar to those previously observed by Gravel et al. (2014) in normally sighted subjects, who found V2 and V3 had similar connective field sizes of ~ 2 mm. Differences between V2 and V3 were small and consisted of connective fields in V2 being smaller than those in V3 for all but the largest eccentricities (Fig. 8, third column, difference

maps). This difference between V2 and V3 was only significant for rsCON_{ox} and stimCON_{uw}, and only the latter result passed correction for multiple comparisons (Table 9).

Connective field size as a function of eccentricity

The bright vertical strips found within Figure 8 (left panels) indicate that connective field sizes remained relatively constant as a function of eccentricity, resembling previous findings that increases in ipsilateral connective field size as a function of eccentricity are small (Haak et al., 2013; Gravel et al., 2014). However, although small, the effects of eccentricity are statistically significant. Standard χ^2 tests of independence found highly significant ($p < 0.01$) interactions between connective field size and eccentricity within both V2 and V3 for every subject group, using both

Table 9. Connective field size estimates: median sizes of connective fields in V2 versus V3, and the results of χ^2 test examining whether the distribution of connective field sizes differed significantly between V2 and V3

Group	Median V2	Median V3	χ^2	p
rsANO _{ox}	2.414	2.438	$\chi^2_{(1,4)} = 2790.331$	0.101
rsCON _{ox}	2.378	2.42	$\chi^2_{(1,6)} = 2928.505^*$	0.013
rsEB _{uw}	2.173	2.078	$\chi^2_{(1,4)} = 2699.013$	0.354
rsCON _{uw}	2.046	2.053	$\chi^2_{(1,4)} = 2728.07$	0.061
stimCON _{uw}	2.285	2.287	$\chi^2_{(1,4)} = 3291.241^{**}$	0.002

*Significant values.

**Statistical values that passed Bonferroni–Holm correction for five comparisons.

Table 10. Group differences in connective field size in V2 and V3

Group	ROI	χ^2	p
ANO _{ox} versus rsCON _{ox}	V2	$\chi^2_{(1,5)} = 2330.462$	0.659
	V3	$\chi^2_{(1,5)} = 2085.337$	0.874
rsEB _{uw} versus rsCON _{uw}	V2	$\chi^2_{(1,4)} = 2913.112^*$	0.066
	V3	$\chi^2_{(1,4)} = 2330.266^*$	0.501
rsCON _{uw} versus stimCON _{uw}	V2	$\chi^2_{(1,4)} = 3578.361^{**}$	0.001
	V3	$\chi^2_{(1,4)} = 4263.147^{**}$	0.000

*Significant values.

**Statistical values that passed Bonferroni–Holm correction for three comparisons.

the group averaged joint probability distributions of Figure 8, and when analyzing each individual hemisphere separately.

Comparison of subject groups found no differences between blind subjects and their sighted controls in the distribution of connective field sizes as a function of eccentricity within either the V2 or the V3 ROI (Table 10). There was a significant difference between resting-state versus visual stimulation in sighted controls within both V2 and V3, which was due to smaller connective fields for resting-state than for stimulus-driven data (see Discussion).

Discussion

Resting-state correlations in occipital cortex

The occipital resting-state signal contains multiple components. One component consists of local spatial correlations, such that BOLD response similarity falls off smoothly as a function of cortical distance, which may reflect spatial spread inherent to the BOLD signal (Engel et al., 1997; Parkes et al., 2005). There are also large-scale iso-eccentric fluctuations within and across hemispheres. These fluctuations are bilaterally symmetric, correlations across hemispheres are stronger for homologous cortical locations representing symmetric regions of visual space (Heinzle et al., 2011; Jo et al., 2012; Butt et al., 2013, 2015; Haak et al., 2013; Gravel et al., 2014; Raemaekers et al., 2014; Arcaro et al., 2015), and may reflect vasculature stemming from the posterior cerebral artery (Tong et al., 2013; Tong and Frederick, 2014). The resting-state component that maps to retinotopic organization, including the polar angle V2/V3 reversal (Heinzle et al., 2011; Gravel et al., 2014; Raemaekers et al., 2014), seems to explain a relatively small proportion of resting-state variance. Our connective fields produced mean correlations between predicted and obtained time courses in V3 that ranged between $r = 0.307$ and $r = 0.416$. Similarly, using resting-state data, Heinzle et al. (2011) reported correlations between predicted and obtained time courses of $r = 0.21$ within V3. In contrast, stimulus-driven data produced correlations of $r = 0.812$ in V3 (Haak et al., 2013).

The connective field method may help emphasize retinotopic components of the resting-state signal, provided care is taken to avoid local minima. Suppose a seed voxel in V2 is strongly corre-

lated with every iso-eccentric location in V1 (due to the bilateral symmetric component) but is most strongly correlated with the location of the same polar angle coordinate. Despite the retinotopic component being relatively weak, the resulting connective field will settle in the location of the retinotopic signal, as this method finds the point of maximum correlation between a seed voxel in V2 and a Gaussian region in V1.

Our finding of retinotopically organized polar angle estimates across the V2/V3 border suggests that our connective field estimates are sensitive to the retinotopic component within the resting-state signal, although it remains unclear to what extent our estimates were also influenced by nonretinotopic components. Possible future directions for better isolating the retinotopic component of the resting-state signal include using longer resting-state sequences or smaller voxel sizes at 7T (Raemaekers et al., 2014), using methods (e.g., independent component analysis) for factoring out non-neural (Tong and Frederick, 2014) or nonretinotopically organized signals, and improved connective field model fitting methods (e.g., global search algorithms) to avoid local minima induced by nonretinotopic components.

Differences between early blind and sighted individuals

One well-established finding, not reexamined in this study, is the observation that early blindness (Bedny et al., 2011; Qin et al., 2013; Burton et al., 2014) and anophthalmia (Watkins et al., 2012) result in a decrease in interhemispheric functional correlations, with the effect of blindness tending to increase across the visual hierarchy. However, there are a number of reasons to believe these interhemispheric correlations reflect iso-eccentric fluctuations rather than retinotopic patterns of connectivity (Bock and Fine, 2014).

An interesting finding of Butt et al. (2015), replicated here, is that although there is little difference in the spatial spread of intrahemispheric spatial correlations between blind and sighted subjects, correlation values in the resting-state signal are higher for early blind subjects compared with sighted controls. One possible explanation is that resting-state firing rates are increased and/or metabolic processes are enhanced within the occipital cortex as a result of early blindness. Dark-reared animals show high spontaneous firing rates within occipital cortex (for review, see Movshon and Van Sluyters, 1981) and early blind individuals show enhanced metabolic activity in occipital cortex, which might enhance the BOLD resting-state signal (Wanet-Defalque et al., 1988; Veraart et al., 1990; Uhl et al., 1993; De Volder et al., 1997; Weaver et al., 2013). Although it is not known whether anophthalmia leads to similar enhancements of metabolic activity and/or resting-state firing, we saw no difference in correlation coefficients between anophthalmic subjects and their sighted controls.

Stimulus-driven versus resting-state connective fields

As seen previously (Heinzle et al., 2011; Gravel et al., 2014; Raemaekers et al., 2014), we found higher correlation coefficients and clearer organization for eccentricity and polar angle in stimulus-driven compared with resting-state data, likely due to larger retinotopically organized neural fluctuations produced by the presence of a visual stimulus.

Similar to Raemaekers et al. (2014), estimated connective fields were smaller for resting-state than for stimulus-driven data within V2 and V3. These size differences are unlikely to be due to lower neural signal in resting-state data because connective field size estimates are an unbiased statistic (Dumoulin and Wandell, 2008; Binda et al., 2013), the reliability of con-

nective field size estimates will be affected by signal-to-noise, but the mean size estimate is robust to signal-to-noise. There are several possible explanations for finding smaller connective fields as follows: (1) the local spatial correlations in the resting-state fMRI signal have a narrower spatial spread compared with the stimulus-driven retinotopic signal (Heinzle et al., 2011; Butt et al., 2013). In the absence of a visual stimulus, these LC would be more influential on the fMRI signal, producing a smaller connective field size. (2) Connective field sizes for stimulus-driven data may be inflated by nonlinear spatiotemporal BOLD interactions. (3) Neural responses related to the predictability of the drifting bar stimulus increase connective field size (Binda et al., 2013). (4) The drifting bar stimulus is weighted toward low spatial frequencies, which might result in BOLD response fluctuations being more influenced by neurons with larger receptive fields (Binda et al., 2013).

If differences in connective field parameters between stimulus-driven and resting-state conditions prove local to cortical regions representing the stimulated visual field, these differences may provide a method for mapping cortical regions with residual visual field function in cognitively impaired individuals with cortical visual impairment. Although collecting MR data in these individuals will generally require sedation, many undergo MR scans for medical reasons. Traditional perimetry tests are often impossible in these individuals, so estimating regions of spared vision is done on the basis of spontaneous behavioral responses, which is difficult and imprecise. Because caregivers are instructed to present items of interest in the spared visual field, an improved ability to estimate spared regions would have clinical value.

Does residual topographic organization interact with cross-modal responses?

We find here that neither retinal waves nor visual experience is necessary for the development and maintenance of retinotopic organization within resting-state signals. This is consistent with an animal literature suggesting that the refinement of intracortical visual circuitry is robust to loss of visual input (Coogan and Van Essen, 1996; Grubb et al., 2003; Cang et al., 2005; Ko et al., 2014). Molecular signaling plays a crucial role in the development of retinotopic maps (Huberman et al., 2008; Cang and Feldheim, 2013), although spontaneous propagating waves of activity within the retina (Demas et al., 2003; McLaughlin et al., 2003) (and possibly the lateral geniculate nucleus, Weliky and Katz, 1999), and postnatal visual experience (Barone et al., 1995; Batardière et al., 2002; Baldwin et al., 2012) play a role in the refinement of these maps.

Nonetheless, it is surprising that retinotopic organization of the resting-state signal persists in blind humans, even after many years of deprivation, especially given the presence of cross-modal responses to auditory and tactile stimuli within these same regions of cortex. As described above, there is a large literature showing occipital cross-modal responses as a result of blindness, and robust cross-modal responses have been previously observed in the particular subjects of this study (Watkins et al., 2013; Jiang et al., 2014). Our results suggest that these cross-modal responses coexist with neural firing patterns that reflect persisting retinotopic organization (also see Striem-Amit et al., 2015).

Cross-modal responses can coexist with visual responses in both occipital cortex and hMT⁺. Sight recovery subject MM was blinded at 3.5 years of age and regained limited vision at 43. Even after sight recovery, MM shows cross-modal re-

sponses within occipital cortex and hMT⁺ (Saenz et al., 2008; Jiang et al., 2014) that coexist with persisting retinotopic organization in occipital cortex (Levin et al., 2010) and visual motion responses in hMT⁺ (Saenz et al., 2008; Jiang et al., 2014).

How might the topographically organized firing patterns observed in our data interact with cross-modal responses? One possibility is that retinotopic responses are orthogonal to cross-modal responses and are merely a persistent artifact of early development. A more interesting possibility is that this topography may influence auditory or tactile responses. Cross-modal auditory motion responses in hMT⁺ responses share topographic similarities with restored visual motion responses: In MM it is possible to use BOLD responses in hMT⁺ to classify the direction of auditory motion stimuli based on a visual motion training set, and vice versa (Jiang et al., 2014). An obvious future direction is to examine whether cross-modal responses (such as auditory frequency tuning or spatial localization) might be topographically aligned with the retinotopic organization within early visual areas.

References

- Ackman JB, Crair MC (2014) Role of emergent neural activity in visual map development. *Curr Opin Neurobiol* 24:166–175. [CrossRef Medline](#)
- Amedi A, Raz N, Pianka P, Malach R, Zohary E (2003) Early 'visual' cortex activation correlates with superior verbal memory performance in the blind. *Nat Neurosci* 6:758–766. [CrossRef Medline](#)
- Arcaro MJ, Honey CJ, Mruczek RE, Kastner S, Hasson U (2015) Widespread correlation patterns of fMRI signal across visual cortex reflect eccentricity organization. *Elife* 4:03952. [CrossRef Medline](#)
- Baldwin MK, Kaskan PM, Zhang B, Chino YM, Kaas JH (2012) Cortical and subcortical connections of V1 and V2 in early postnatal macaque monkeys. *J Comp Neurol* 520:544–569. [CrossRef Medline](#)
- Barone P, Dehay C, Berland M, Bullier J, Kennedy H (1995) Developmental remodeling of primate visual cortical pathways. *Cereb Cortex* 5:22–38. [CrossRef Medline](#)
- Batardière A, Barone P, Knoblauch K, Giroud P, Berland M, Dumas AM, Kennedy H (2002) Early specification of the hierarchical organization of visual cortical areas in the macaque monkey. *Cereb Cortex* 12:453–465. [CrossRef Medline](#)
- Bedny M, Pascual-Leone A, Dodell-Feder D, Fedorenko E, Saxe R (2011) Language processing in the occipital cortex of congenitally blind adults. *Proc Natl Acad Sci U S A* 108:4429–4434. [CrossRef Medline](#)
- Benson NC, Butt OH, Datta R, Radoeva PD, Brainard DH, Aguirre GK (2012) The retinotopic organization of striate cortex is well predicted by surface topology. *Curr Biol* 22:2081–2085. [CrossRef Medline](#)
- Benson NC, Butt OH, Brainard DH, Aguirre GK (2014) Correction of distortion in flattened representations of the cortical surface allows prediction of V1–V3 functional organization from anatomy. *PLoS Comput Biol* 10:e1003538. [CrossRef Medline](#)
- Binda P, Thomas JM, Boynton GM, Fine I (2013) Minimizing biases in estimating the reorganization of human visual areas with BOLD retinotopic mapping. *J Vis* 13:13. [CrossRef Medline](#)
- Biswal B, Yetkin FZ, Haughton VM, Hyde JS (1995) Functional connectivity in the motor cortex of resting human brain using echo-planar MRI. *Magn Reson Med* 34:537–541. [CrossRef Medline](#)
- Bock AS, Fine I (2014) Anatomical and functional plasticity in early blind individuals and the mixture of experts architecture. *Front Hum Neurosci* 8:971. [CrossRef Medline](#)
- Bowman FD, Zhang L, Derado G, Chen S (2012) Determining functional connectivity using fMRI data with diffusion-based anatomical weighting. *Neuroimage* 62:1769–1779. [CrossRef Medline](#)
- Brainard DH (1997) The Psychophysics Toolbox. *Spat Vis* 10:433–436. [CrossRef Medline](#)
- Burton H, Snyder AZ, Raichle ME (2014) Resting state functional connectivity in early blind humans. *Front Syst Neurosci* 8:51. [CrossRef Medline](#)
- Butt OH, Benson NC, Datta R, Aguirre GK (2013) The fine-scale functional correlation of striate cortex in sighted and blind people. *J Neurosci* 33:16209–16219. [CrossRef Medline](#)

- Butt OH, Benson NC, Datta R, Aguirre GK (2015) Hierarchical and homotopic correlations of spontaneous neural activity within the visual cortex of the sighted and blind. *Front Hum Neurosci* 9:25. [CrossRef Medline](#)
- Cang J, Feldheim DA (2013) Developmental mechanisms of topographic map formation and alignment. *Annu Rev Neurosci* 36:51–77. [CrossRef Medline](#)
- Cang J, Rentería RC, Kaneko M, Liu X, Copenhagen DR, Stryker MP (2005) Development of precise maps in visual cortex requires patterned spontaneous activity in the retina. *Neuron* 48:797–809. [CrossRef Medline](#)
- Collignon O, Voss P, Lassonde M, Lepore F (2009) Cross-modal plasticity for the spatial processing of sounds in visually deprived subjects. *Exp Brain Res* 192:343–358. [CrossRef Medline](#)
- Coogan TA, Van Essen DC (1996) Development of connections within and between areas V1 and V2 of macaque monkeys. *J Comp Neurol* 372:327–342. [CrossRef Medline](#)
- Dale AM, Fischl B, Sereno MI (1999) Cortical surface-based analysis: I. Segmentation and surface reconstruction. *Neuroimage* 9:179–194. [CrossRef Medline](#)
- Davey CE, Grayden DB, Egan GF, Johnston LA (2013) Filtering induces correlation in fMRI resting state data. *Neuroimage* 64:728–740. [CrossRef Medline](#)
- Dehay C, Horsburgh G, Berland M, Killackey H, Kennedy H (1989) Maturation and connectivity of the visual cortex in monkey is altered by prenatal removal of retinal input. *Nature* 337:265–267. [CrossRef Medline](#)
- Dehay C, Giroud P, Berland M, Killackey H, Kennedy H (1996) Contribution of thalamic input to the specification of cytoarchitectonic cortical fields in the primate: effects of bilateral enucleation in the fetal monkey on the boundaries, dimensions, and gyrification of striate and extrastriate cortex. *J Comp Neurol* 367:70–89. [CrossRef Medline](#)
- Della-Maggiore V, Chau W, Peres-Neto PR, McIntosh AR (2002) An empirical comparison of SPM preprocessing parameters to the analysis of fMRI data. *Neuroimage* 17:19–28. [CrossRef Medline](#)
- Demas J, Eglén SJ, Wong RO (2003) Developmental loss of synchronous spontaneous activity in the mouse retina is independent of visual experience. *J Neurosci* 23:2851–2860. [Medline](#)
- De Volder AG, Bol A, Blin J, Robert A, Arno P, Grandin C, Michel C, Veraart C (1997) Brain energy metabolism in early blind subjects: neural activity in the visual cortex. *Brain Res* 750:235–244. [CrossRef Medline](#)
- Dougherty RF, Koch VM, Brewer AA, Fischer B, Modersitzki J, Wandell BA (2003) Visual field representations and locations of visual areas V1/2/3 in human visual cortex. *J Vis* 3:586–598. [Medline](#)
- Dumoulin SO, Wandell BA (2008) Population receptive field estimates in human visual cortex. *Neuroimage* 39:647–660. [CrossRef Medline](#)
- Duncan RO, Boynton GM (2003) Cortical magnification within human primary visual cortex correlates with acuity thresholds. *Neuron* 38:659–671. [CrossRef Medline](#)
- Engel SA, Glover GH, Wandell BA (1997) Retinotopic organization in human visual cortex and the spatial precision of functional MRI. *Cereb Cortex* 7:181–192. [CrossRef Medline](#)
- Fine I, Wade AR, Brewer AA, May MG, Goodman DF, Boynton GM, Wandell BA, MacLeod DI (2003) Long-term deprivation affects visual perception and cortex. *Nat Neurosci* 6:915–916. [CrossRef Medline](#)
- Fischl B, Sereno MI, Tootell RB, Dale AM (1999) High-resolution intersubject averaging and a coordinate system for the cortical surface. *Hum Brain Mapp* 8:272–284. [CrossRef Medline](#)
- Gravel N, Harvey B, Nordhjem B, Haak KV, Dumoulin SO, Renken R, Curéïa-Blake B, Cornelissen FW (2014) Cortical connective field estimates from resting state fMRI activity. *Front Neurosci* 8:339. [CrossRef Medline](#)
- Greicius MD, Krasnow B, Reiss AL, Menon V (2003) Functional connectivity in the resting brain: a network analysis of the default mode hypothesis. *Proc Natl Acad Sci U S A* 100:253–258. [CrossRef Medline](#)
- Greicius MD, Supekar K, Menon V, Dougherty RF (2009) Resting-state functional connectivity reflects structural connectivity in the default mode network. *Cereb Cortex* 19:72–78. [CrossRef Medline](#)
- Greve D, Sabuncu M, Shafiq R, Schmansky N, Buckner R, Fischl B (2011) Automatic surface-based interhemispheric registration with FreeSurfer. [OHBM Abstract](#).
- Grubb MS, Rossi FM, Changeux JP, Thompson ID (2003) Abnormal functional organization in the dorsal lateral geniculate nucleus of mice lacking the beta 2 subunit of the nicotinic acetylcholine receptor. *Neuron* 40:1161–1172. [CrossRef Medline](#)
- Haak KV, Winawer J, Harvey BM, Renken R, Dumoulin SO, Wandell BA, Cornelissen FW (2013) Connective field modeling. *Neuroimage* 66:376–384. [CrossRef Medline](#)
- Hagmann P, Cammoun L, Gigandet X, Meuli R, Honey CJ, Wedeen VJ, Sporns O (2008) Mapping the structural core of human cerebral cortex. *PLoS Biol* 6:0060159. [CrossRef Medline](#)
- Heinzle J, Kahnt T, Haynes JD (2011) Topographically specific functional connectivity between visual field maps in the human brain. *Neuroimage* 56:1426–1436. [CrossRef Medline](#)
- Hirsch HV, Leventhal AG (1978) Functional modification of the developing visual system. In: *Development of sensory systems*, pp 279–335. New York: Springer.
- Hogstrom LJ, Westlye LT, Walhovd KB, Fjell AM (2013) The structure of the cerebral cortex across adult life: age-related patterns of surface area, thickness, and gyrification. *Cereb Cortex* 23:2521–2530. [CrossRef Medline](#)
- Holm S (1979) A simple sequentially rejective multiple test procedure. *Scand J Stat* 6:65–70.
- Honey CJ, Sporns O, Cammoun L, Gigandet X, Thiran JP, Meuli R, Hagmann P (2009) Predicting human resting-state functional connectivity from structural connectivity. *Proc Natl Acad Sci U S A* 106:2035–2040. [CrossRef Medline](#)
- Huberman AD, Feller MB, Chapman B (2008) Mechanisms underlying development of visual maps and receptive fields. *Annu Rev Neurosci* 31:479–509. [CrossRef Medline](#)
- Jiang F, Stecker GC, Fine I (2014) Auditory motion processing after early blindness. *J Vis* 14:4. [CrossRef Medline](#)
- Jo HJ, Saad ZS, Simmons WK, Milbury LA, Cox RW (2010) Mapping sources of correlation in resting state fMRI, with artifact detection and removal. *Neuroimage* 52:571–582. [CrossRef Medline](#)
- Jo HJ, Saad ZS, Gotts SJ, Martin A, Cox RW (2012) Quantifying agreement between anatomical and functional interhemispheric correspondences in the resting brain. *PLoS One* 7:8. [CrossRef Medline](#)
- Ko H, Mrcic-Flogel TD, Hofer SB (2014) Emergence of feature-specific connectivity in cortical microcircuits in the absence of visual experience. *J Neurosci* 34:9812–9816. [CrossRef Medline](#)
- Levin N, Dumoulin SO, Winawer J, Dougherty RF, Wandell BA (2010) Cortical maps and white matter tracts following long period of visual deprivation and retinal image restoration. *Neuron* 65:21–31. [CrossRef Medline](#)
- Lewis LB, Fine I (2011) The effects of visual deprivation after infancy. In: *Adler's physiology of the eye*, Ed 11 (Levin LA, Nilsson SFE, Ver Hoeve J, Wu SM, eds), pp 750–767. Amsterdam: Elsevier.
- McHugh ML (2013) The chi-square test of independence. *Biochem Med* 23:143–149. [CrossRef Medline](#)
- McLaughlin T, Torborg CL, Feller MB, O'Leary DD (2003) Retinotopic map refinement requires spontaneous retinal waves during a brief critical period of development. *Neuron* 40:1147–1160. [CrossRef Medline](#)
- Movshon JA, Van Sluyters RC (1981) Visual neural development. *Annu Rev Psychol* 32:477–522. [CrossRef Medline](#)
- Parkes LM, Schwarzbach JV, Bouts AA, Deckers RH, Pullens P, Kerskens CM, Norris DG (2005) Quantifying the spatial resolution of the gradient echo and spin echo BOLD response at 3 Tesla. *Magn Reson Med* 54:1465–1472. [CrossRef Medline](#)
- Pelli DG (1997) The VideoToolbox software for visual psychophysics: transforming numbers into movies. *Spat Vis* 10:437–442. [CrossRef Medline](#)
- Qin W, Liu Y, Jiang T, Yu C (2013) The development of visual areas depends differently on visual experience. *PLoS One* 8:e53784. [CrossRef Medline](#)
- Raemaekers M, Schellekens W, van Wezel RJ, Petridou N, Kristo G, Ramsey NF (2014) Patterns of resting state connectivity in human primary visual cortical areas: a 7T fMRI study. *Neuroimage* 84:911–921. [CrossRef Medline](#)
- Rao MS, Jacobson M (2006) *Developmental neurobiology*. New York: Springer.
- Saenz M, Lewis LB, Huth AG, Fine I, Koch C (2008) Visual motion area MT+ /V5 responds to auditory motion in human sight-recovery subjects. *J Neurosci* 28:5141–5148. [CrossRef Medline](#)
- Sathian K, Stilla R (2010) Cross-modal plasticity of tactile perception in blindness. *Restor Neurol Neurosci* 28:271–281. [CrossRef Medline](#)
- Sherman SM, Spear PD (1982) Organization of visual pathways in normal and visually deprived cats. *Physiol Rev* 62:738–855. [Medline](#)
- Sikl R, Simeček M, Porubánová-Norquist M, Bezdišek O, Kremláček J,

- Stodůlka P, Fine I, Ostrovsky Y (2013) Vision after 53 years of blindness. *Perception* 42:498–507. [CrossRef Medline](#)
- Skudlarski P, Constable RT, Gore JC (1999) ROC analysis of statistical methods used in functional MRI: individual subjects. *Neuroimage* 9:311–329. [CrossRef Medline](#)
- Striem-Amit E, Ovidia-Caro S, Caramazza A, Margulies DS, Villringer A, Amedi A (2015) Functional connectivity of visual cortex in the blind follows retinotopic organization principles. *Brain* 138:1679–1695. [CrossRef Medline](#)
- Strother SC (2006) Evaluating fMRI preprocessing pipelines. *IEEE Eng Med Biol Mag* 25:27–41. [CrossRef Medline](#)
- Tong Y, Frederick BD (2014) Tracking cerebral blood flow in BOLD fMRI using recursively generated regressors. *Hum Brain Mapp* 35:5471–5485. [CrossRef Medline](#)
- Tong Y, Hocke LM, Nickerson LD, Licata SC, Lindsey KP, Frederick Bd (2013) Evaluating the effects of systemic low frequency oscillations measured in the periphery on the independent component analysis results of resting state networks. *Neuroimage* 76:202–215. [CrossRef Medline](#)
- Uhl F, Franzen P, Podreka I, Steiner M, Deecke L (1993) Increased regional cerebral blood flow in inferior occipital cortex and cerebellum of early blind humans. *Neurosci Lett* 150:162–164. [CrossRef Medline](#)
- Veraart C, De Volder AG, Wanet-Defalque MC, Bol A, Michel C, Goffinet AM (1990) Glucose utilization in human visual cortex is abnormally elevated in blindness of early onset but decreased in blindness of late onset. *Brain Res* 510:115–121. [CrossRef Medline](#)
- Wanet-Defalque MC, Veraart C, De Volder A, Metz R, Michel C, Doooms G, Goffinet A (1988) High metabolic activity in the visual cortex of early blind human subjects. *Brain Res* 446:369–373. [CrossRef Medline](#)
- Watkins KE, Cowey A, Alexander I, Filippini N, Kennedy JM, Smith SM, Ragge N, Bridge H (2012) Language networks in anophthalmia: maintained hierarchy of processing in ‘visual’ cortex. *Brain* 135:1566–1577. [CrossRef Medline](#)
- Watkins KE, Shakespeare TJ, O’Donoghue MC, Alexander I, Ragge N, Cowey A, Bridge H (2013) Early auditory processing in area V5/MT+ of the congenitally blind brain. *J Neurosci* 33:18242–18246. [CrossRef Medline](#)
- Weaver KE, Richards TL, Saenz M, Petropoulos H, Fine I (2013) Neurochemical changes within human early blind occipital cortex. *Neuroscience* 252:222–233. [CrossRef Medline](#)
- Weliky M, Katz LC (1999) Correlational structure of spontaneous neuronal activity in the developing lateral geniculate nucleus in vivo. *Science* 285:599–604. [CrossRef Medline](#)